Electronic Supplementary Material (ESI) for Chemical Communications.

Recycling cobalt in spent lithium ion batteries to design CoN/HPCF/CoN electrocatalysts for advanced zinc-air batteries

Yibin Wang[a], Lan Xiao[a], Yingjie Zhang[a], Mian Li[a, *], Tingting Liu[b, c, *]

[a] National and Local Joint Engineering Center for Lithium-ion Batteries and Materials Preparation Technology, Faculty of Metallurgical and Energy Engineering, Kunming University of Science and Technology, Kunming 650093, PR China.

[b] School of Materials and Energy, Yunnan University, No. 2, Green Lake North Road, Kunming 650091, PR China.

[c] Electron Microscopy Center, Yunnan University, No. 2, Green Lake North Road, Kunming 650091, PR China.

* Corresponding author:
E-mail address: lim148@kmust.edu.cn, mianzi2009@126.com (M. Li); liutt133@ynu.edu.cn (T. Liu).

1. Experimental Section

1.1. Recycling Co as cobalt oxalate from the spent lithium cobalt oxide (LCO) based lithium-ion batteries (LIBs).

The spent LCO batteries (obtained from Brunp Co., Ltd) were first immersed to release residual electricity (in saturated NaCl solution, for 24 h). The aluminum shells were then dismantled to get electric cores. Whereafter, the as prepared positive electrodes were separated and washed with N-methylpyrrolidone (NMP). After a filtration process, the resultant products were calcined in air at 700 ℃ for 4 h to remove the carbon and residuary organic matters. The resultant LCO material was leached by using the mild organic acids (glycine & ascorbic acid) at 85 ℃. After a secondary filtration process, the oxalic acid were added to precipitate the Co(II) as cobalt oxalates [S1].

1.2. Recycling the hollow and porous carbon nanofibers (HPCF) from the catkin biomass.

The catkin biomass (obtained from Kunming) was first collected from the willows and washed with deionized water. Then, the resultant catkin floccules were eliminated the solid particles and calcined in nitrogen (N_2) atmosphere at 900 ℃ for 2 h to get the HPCF matrixes.

1.3. Synthesizing the pure CoN and CoN/HPCF/CoN catalysts.

For synthesizing the precursor of CoN/HPCF/CoN, 200 mg of HPCF carbon matrices, 400 mg of cobalt acetate, and 20 mmol of hexamethylenetetramine (HMT) were first dissolved in 100 mL of distilled water under vigorous stirring for 2 h to form the uniform mixture slurries. Then, the as-prepared mixture slurry was thoroughly transferred into 120 mL Teflon-lined autoclave and heated at 120 °C for another 12 h. After the Teflon-lined autoclave was cooled to room temperature, the as-collected products were washed with water and ethanol for several times. After centrifuging the resultant mixture solutions and dried the resultant matters in a vacuum overnight, the precursor of CoN/HPCF/CoN was successfully prepared. To prepare the precursor of pure CoN, the procuresses and conditions were the same as those for preparing the precursor of CoN/HPCF/CoN, the only difference is that no any carbon matrix was added into the mixture slurry.

To synthesize the pure CoN and CoN/HPCF/CoN electrocatalysts, the as-prepared precursors were severally placed in the porcelain boats and heated in the tube at 400 °C (with a rate of 5 °C min^{-1}) in the NH_3 atmosphere.

1.4. The physical characterization of resultant catalysts.

The wide-angle X-ray diffraction (XRD) patterns were obtained on an X-ray D/max-2200 vpc (Rigaku Corporation, Japan) instrument operated at 40 kV and 20 mA using Cu Kα radiation (k 0.15406 nm). The scanning electron microscopy (SEM)

was performed using a Philips XL-30 ESEM. The transmission electron microscopy (TEM), high-angle annular dark field scanning transmission electron microscopy (HAADF-STEM), and scanning transmission electron microscopy (STEM) were performed on a high-resolution Hitachi JEM-2100 system equipped with an EDX analyzer. The surface analyses of various catalysts were carried out by X-ray photoelectron spectroscopy (XPS) on an ESCA LAB spectrometer (USA) using a monochromatic Al Kα source (*hv* 1486.6 eV). The binding energies were calibrated by using the containment carbon (C1s 284.6 eV). The N_2 adsorption-desorption isotherms were performed on an ASAP 2020 instrument (Micromeritics, USA). Before the measurements, all samples were first degassed in vacuum at 140 °C for 6 h. The Brunauer-Emmett-Teller (BET) method was utilized to calculate the BET specific surface area using adsorption data. The pore size distribution was derived from the adsorption branch by using the Barrett-Joyner-Halenda (BJH) model. Raman spectra were obtained using a confocal microprobe Raman system (HR800, JobinYvon).

1.5. The electrochemical measurement of resultant catalysts.

All electrochemical measurements referring to oxygen reduction reaction (ORR) and oxygen evolution reaction (OER) were performed with a standard three-electrode cell at room temperature by using the rotating disk electrode (RDE) or rotating ring disk electrode (RRDE) modified by as-synthesized electrocatalysts as the working electrode (5 mm in diameter, 0.19625 cm^2). The commercial Hg/HgO electrode was used as reference electrode and the commercial Pt wire was used as counter electrode for OER/ORR test. All potentials appeared in this paper are referred to the reversible hydrogen electrode (RHE) and all potentials recorded referring to Hg/HgO in each experiment were calculated using the **eqn. S1** as follows:

$$E_{RHE} = E_{Hg/HgO} + 0.059\ pH + 0.098\ V \qquad (\mathbf{S1})$$

In **eqn. S1**, the E_{RHE} values are the potentials *vs.* RHE, $E_{Hg/HgO}$ values are the potentials *vs.* Hg/HgO electrode, and pH is the pH value of electrolyte (1.0 M KOH solution, pH = 14). All current densities are the ratios of recorded currents to the geometric area of electrode. The linear sweep voltammetry (LSV) curves were recorded with *iR* drop compensation unless specifically mentioned.

In order to prepare the working electrodes, 3 mg of catalyst powders were firstly dispersed in 1 mL Nafion solution (0.5 wt%) with 45 min of ultrasonication to generate homogeneous inks. Next, 30 uL of the dispersion was transferred onto the RDE or RRDE with the catalyst loading amount of 0.306 mg cm^{-2}. Finally, the as-prepared catalyst film was dried at room temperature.

In the electrochemical testing processes of ORR and OER, the polarization curves were plotted as potential (E/V) *vs.* log $|j$ / mA $cm^{-2}|$ to get the Tafel plots for assessing the ORR/OER kinetics of resultant catalysts. By fitting the linear portion of the Tafel plots to the Tafel **equ. S2**, the Tafel slopes (i.e. the b values) can be obtained.

$$\eta = b \log (j) + a \qquad (\mathbf{S2})$$

For the ORR test, the apparent electron transfer numbers (n) and H_2O_2 yields (%) during the ORR processes were tested by the RRDE measurements. The operating potential of Pt ring on RRDE was set as 0.5 V *vs.* Hg/HgO. Using the as-measured RRDE data, corresponding n values were calculated through **eqn. S3** and H_2O_2 yields were calculated through **eqn. S4**:

$$n = \frac{4I_D}{(I_D + I_R / N)} \quad \textbf{(S3)}$$

$$\% \ HO_2^- = \frac{200I_R)}{(I_D N + I_R)} \quad \textbf{(S4)}$$

What needs illustration is that, in **eqn. S3** and **eqn. S4**, N is the collection efficiency of used RRDE system (0.37), I_D and I_R are the as-recorded faradic-disk and ring current values, respectively.

The Zn-air battery (ZAB) performances were tested in home-made electrochemical cell (a traditional liquid rechargeable zinc-air battery), which was constituted by the electrolyte [6 M KOH solution with 0.2 M $Zn(Ac)_2$], the current collectors (nickel foam), a polished zinc plate and a catalyst layer coated gas diffusion electrode. To prepare the air-electrode, 3 mg of catalyst was dispersed in 6 mL of ethanol with adding 50 μL of Nafion solution. After 2 h of ultrasonic treatment, 2 mL of the ink was sprayed onto a carbon paper (1 cm × 1 cm) with affording a loading amount of 1 mg cm^{-2}. For comparison, another ZAB was constructed by using commercial 20 *wt*% Pt/C + IrO2 (loading: 0.25 mg cm^{-2}) mixture catalyst through the same method.

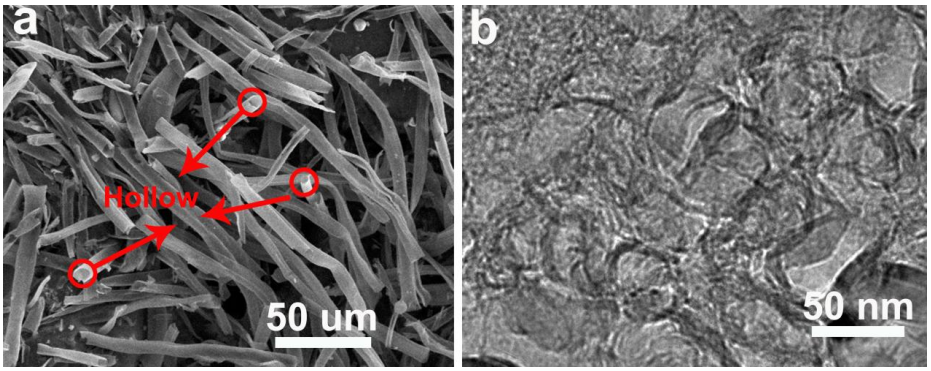

Fig. S1. SEM (**a**) and TEM (**b**) images of the as-prepared HPCF matrixes.

One can see from **Fig. S1** that the HPCF matrixes are all hollow and porous carbon fibers with diameters between 5 and 10 μm. The SEM image of HPCF (**Fig. S1a**) can clearly observe the hollow channels from the top areas and the TEM image of HPCF (**Fig. S1b**) reveals the extensive dispersion of abundant mesopores between 2 and 50 nm along the surfaces of HPCF matrixes. These porous structures are mainly rooted in the continuous release of H_2O and/or CO_2 gases during the carbonation process of plant biomass−catkin (*i.e.,* the precursor of HPCF matrixes).

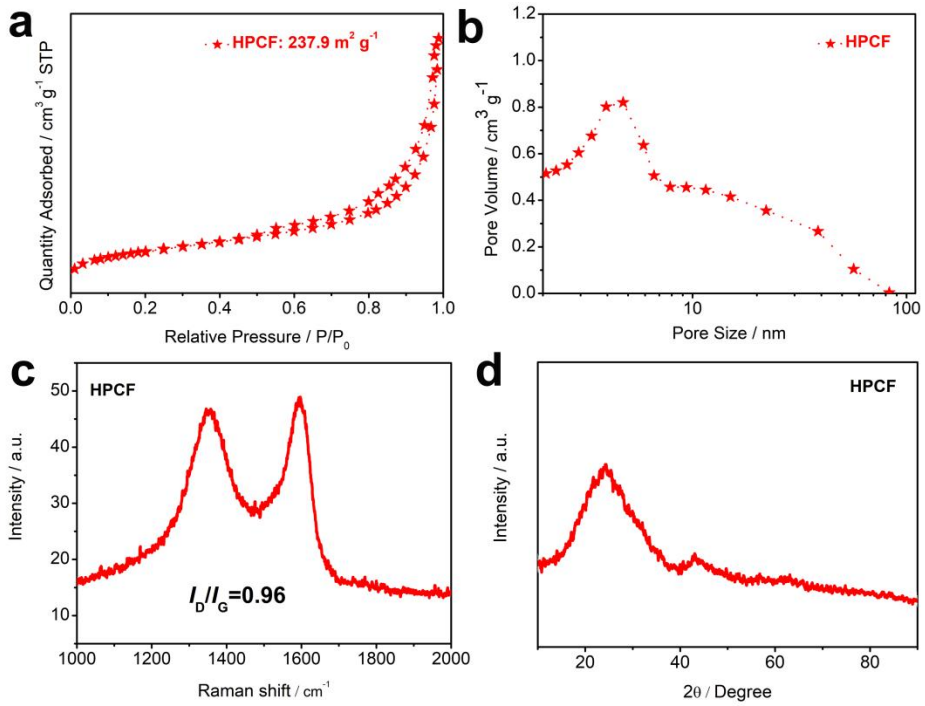

Fig. S2. The corresponding nitrogen (N_2) adsorption–desorption isotherm (**a**), pore-size distribution plot (**b**), Raman spectrum (**c**), and XRD pattern (**d**) of the HPCF matrix.

The N_2 adsorption-desorption isotherm (**Fig. S2a**) display that the HPCF matrix affords a large BET specific surface area of 237.9 m^2 g^{-1}. In addition, the pore size distribution status of HPCF matrix was obtained using desorption branch of isotherm by the BJH method (**Fig. S2b**). As two contactable surfaces coexist on both the inner

and outer walls simultaneously, the HPCF can afford more mesoporous structures and carbon edges. As shown in **Fig. S2c**, the Raman spectrum of HPCF matrix displays the strong D peak and G peak with showing a rarely high intensity ratio of D to G (I_D/I_G) of 0.96; which proves a high defect density of HPCF matrix. The XRD pattern of HPCF matrix (as shown in **Fig. S2d)** displays two diffraction peaks located at ~26° and ~43.5°, being ascribed to the hexagonally graphitic structures. All these characterization results collectively show that the typical hollow tube-like structure and abundant mesopores dispersed along both the outer and inner surfaces of HPCF can really afford a larger surface area as well more carbon edges/defects, which are in favor of dispersing more tiny and effective active sites and meanwhile regulating the sizes of active nanoparticles.

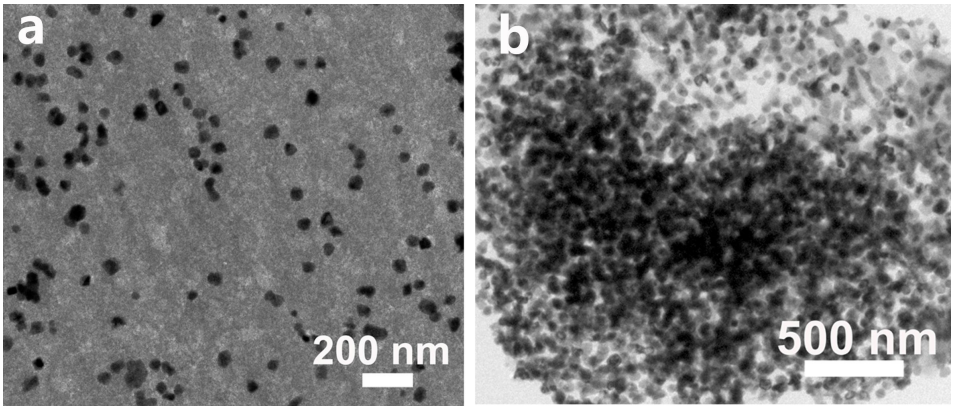

Fig. S3. The TEM images of independently dispersed nanoparticles **(a)** and large clusters **(b)** on CoN/HPCF/CoN;

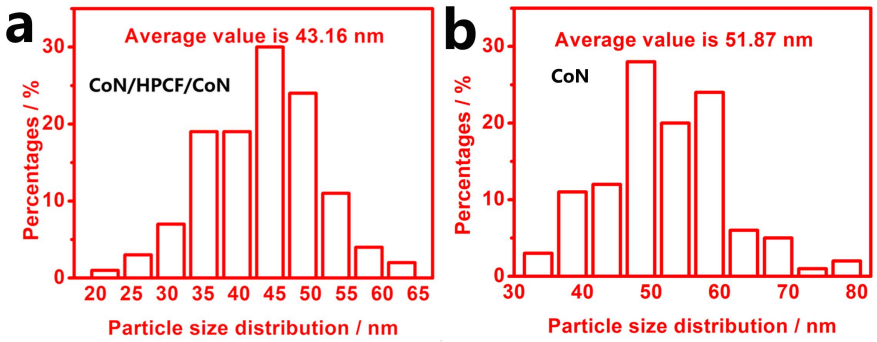

Fig. S4. Histograms of particle size distribution of CoN nanoparticles for pure CoN samples. The histograms of particle size distribution were obtained by counting on the micrographs at least 300 nanoparticles.

As shown in **Fig. S4a,** the histogram of CoN nanoparticle size distribution for CoN/HPCF/CoN revealed that after the nitridation process, the particle sizes of most CoN nanoparticles were smaller than 55 nm (mainly located between 30-55 nm) with providing an average particle diameter of 43.16 nm. Nevertheless, the histogram of CoN nanoparticle size distribution for pure CoN sample (**Fig. S4b**) revealed that most CoN nanoparticles were located between 35-70 nm with a larger average particle diameter of 51.87 nm in comparation to the CoN/HPCF/CoN. The corresponding

conclusion disclosed that the well-dispersed mesopores and abundant carbon edges/defects formed along both inner and outer walls of HPCF matrix can lead to a large BET surface area and boost the dispersing and coupling of tiny CoN nanoparticles.

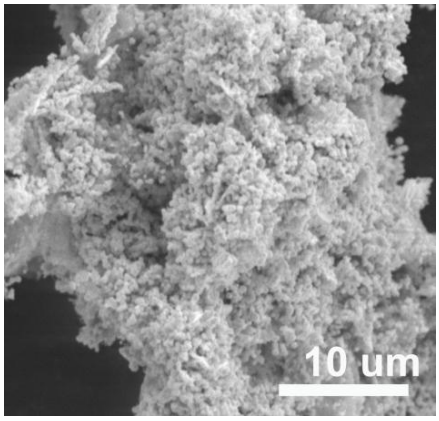

Fig. S5. The SEM image of the as-prepared pure CoN sample.

As described in **Fig. S5,** without using the HPCF as matrix, the SEM image of resultant pure CoN sample proves that the pure CoN sample is bulky material randomly piled by some secondary nanoparticles.

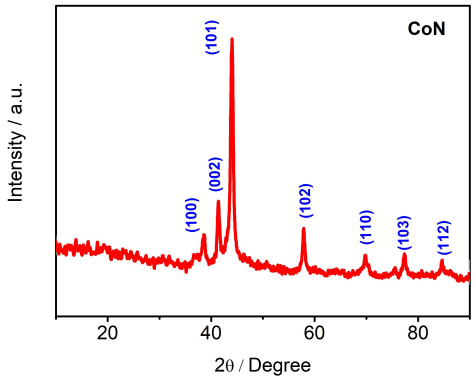

Fig. S6. The XRD pattern of the pure CoN sample.

The XRD pattern of resultant pure CoN sample is showed in **Fig. S6**, the peaks located at 39.05°, 41.58°, 44.37°, 58.15°, 70.72°, 77.70°, and 85.39° are assigned to the (100), (002), (101), (102), (110), (103), and (112) facets of pure $Co_2N_{0.67}$ phase (JCPDS: No. 06-0691), which are similar to those observed on CoN/HPCF/CoN and indicate the successful formation of $Co_2N_{0.67}$ *via* the nitrogen treatment. Nevertheless, no any diffraction peak of graphitic carbon has been found.

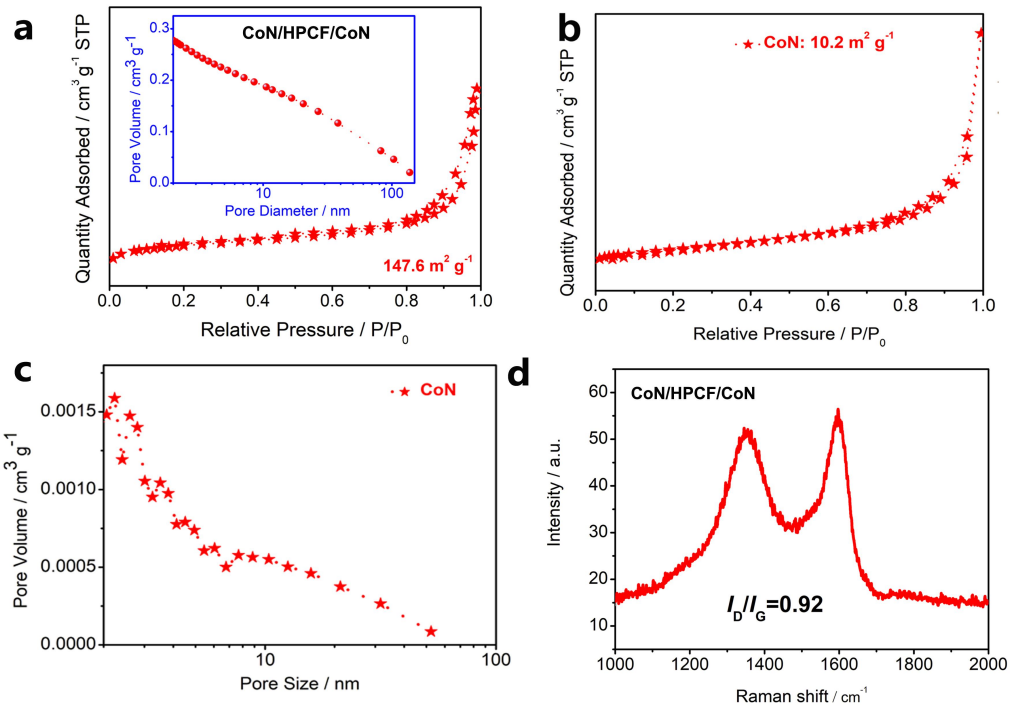

Fig. S7. The N_2 adsorption–desorption isotherm **(a)** and pore size distribution plot (**inset of a**) of CoN/HPCF/CoN hybrid sample. The N_2 adsorption–desorption isotherm **(b)** and corresponding pore size distribution plot **(c)** of pure CoN sample. The Raman spectrum **(d)** of CoN/HPCF/CoN hybrid sample.

N_2 adsorption-desorption isotherm (**Fig. S7b**) display that the pure CoN sample prepared without using HPCF as matrix just displays a fairly small BET specific surface area of 10.2 m^2 g^{-1}. In addition, the corresponding pore-size distribution result (**Fig. S7c**) of pure CoN sample was obtained using desorption branch of isotherm by the BJH method. As the close-packed structure of CoN secondary particles, the pure CoN sample just owns a small number of mesopores located between 2-50 nm.

The Raman spectrum of CoN/HPCF/CoN hybrid sample displays the strong D peak and G peak with showing a D to G intensity ratio (I_D/I_G) of 0.92 (as shown in **Fig. S7d**). It is clear that the I_D/I_G value of CoN/HPCF/CoN is a little smaller than that of HPCF matrix (0.96; as shown in **Fig. S2c**), which proves that the CoN nanoparticles have dispersed surrounding the mesopores and carbon edges dispersed along both inner and outer walls of HPCF matrix.

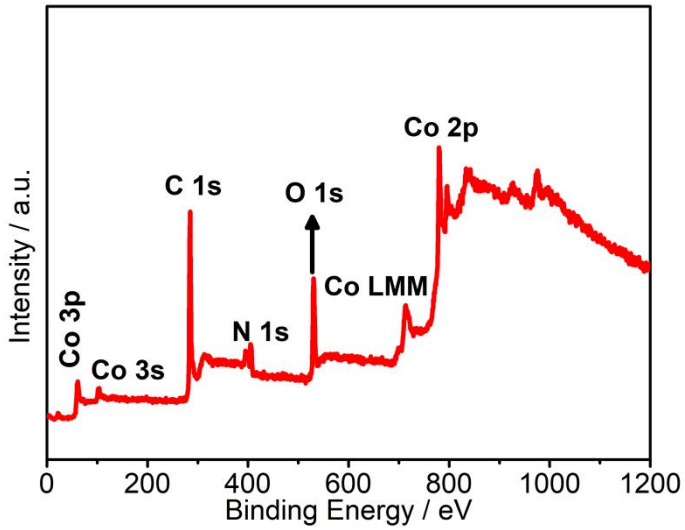

Fig. S8. The XPS survey spectrum of CoN/HPCF/CoN hybrid sample.

The elemental/chemical composition and valence state of the CoN/HPCF/CoN hybrid sample were tested by using XPS. XPS survey spectrum (**Fig. S8**) reveals the existence of C, N, O, and Co elements in the CoN/HPCF/CoN hybrid sample.

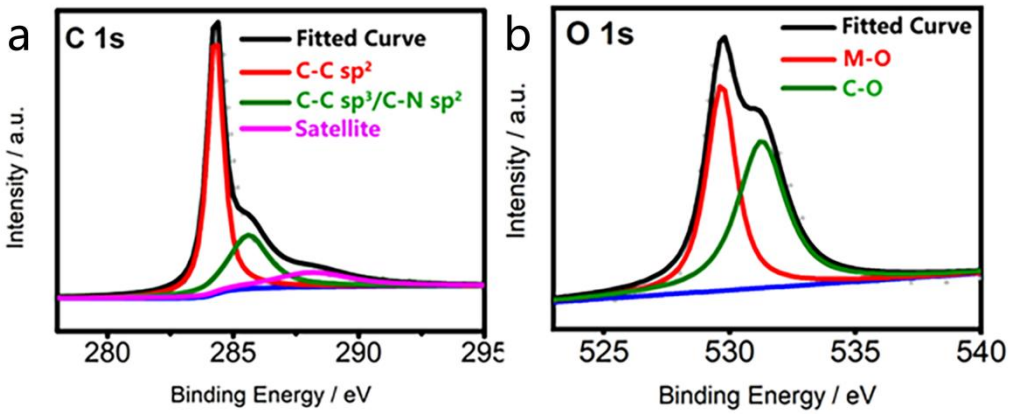

Fig. S9. The high-resolution C 1s **(a)** and O 1s **(b)** spectra of resultant CoN/HPCF/CoN hybrid sample.

As shown in **Fig. S9a,** the high-resolution C 1s XPS spectrum of CoN/HPCF/CoN hybrid sample exhibits a main peak and two weak peaks, which are assigned to the C-C sp^2 (~284.5 eV), C-C sp^3/C-N sp^2 (~285.6 eV), and C-O (~287.6 eV) peaks. As shown in **Fig. S9b,** the high-resolution O 1s XPS spectrum of CoN/HPCF/CoN hybrid sample can be segmented into two characteristic peaks of C-O (~531.5 eV) and C-OH (~533.2 eV) species. The high-resolution O 1s XPS reveals that most CoN nanoparticles dispersed on HPCF matrixes were underwent negligible surface oxidation.

Table S1 A comparison on ORR catalytic parameters between our catalysts and other as-reported non-precious metal based ORR catalysts.

Catalyst	$E_{1/2}$ (V *vs.* RHE)	Tafel slope (mV dec^{-1})	References
Pure HPCF	0.793	45.53	**This Work**
Pure CoN	0.805	40.46	
CoN/HPCF/CoN	**0.828**	**34.87**	
20 wt% Pt/C	0.841	37.52	
Co_2P/CoNPC	0.843	58.2	Adv. Mater. 2020;32(36):2003649.
CoFe/N-GCT	0.79	71	Angew. Chem. Int. Ed. 2018:57(49):16166-16170.
CoZn-NC-700	0.84	60	Adv. Funct. Mater. 2017;27(37):1700795.
Co/N CCPC-3	0.827	63	Nano Energy. 2021;79:105487.
CoN-HPCNF-900	0.81	72	Chem. Eng. J. 2021;407:127157.
Co_4N@NC-2	0.84	64.92	Appl. Catal. B: Environ. 2020;275:119104.
Co-N-C-10	0.79	50.7	Nano Energy. 2018;46:396-403.
Co-ISAS/p-CN	0.838	61	Adv. Mater. 2018;30(15):1706508.
SC CoO	0.85	47	Nat. Commun. 2016;7:12876.
Fe-Co_4N@N-C	0.83	58	Appl. Catal. B: Environ. 256 (2019) 117893.
CoS_x/Co-NC-800	0.80	62	Adv. Funct. Mater. 29 (2019) 1904481.
CoSAs/PTFs	0.81	57	J. Mater. Chem. A, 7 (2019) 1252-1259.

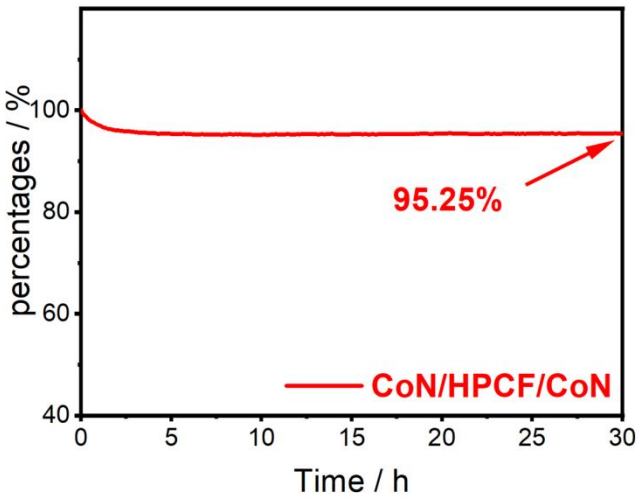

Fig. S10. The chronoamperometry measurement (*I*–*t*) of CoN/HPCF/CoN hybrid sample toward ORR carried out at 0.6 V vs. RHE for 30 h in 1.0 M KOH.

Table S2 A comparison on OER catalytic parameters between our resultant catalysts and other as-reported non-precious metal based OER catalysts.

Catalyst	E_{10} (V *vs.* RHE)	Tafel slope (mV dec^{-1})	References
Pure HPCF	1.756	72.53	**This work**
Pure CoN	1.583	45.46	
CoN/HPCF/CoN	**1.531**	**35.61**	
IrO_2	1.566	59.53	
Co_4N	1.56	58	Inorg. Chem. Front., 2016, 3, 236–242
CoN	1.52	70	Angew.Chem. Int. Ed. 2016, 55,8670 –8674
CoN-Gr	1.51	68.83	Journal of Energy Chemistry 62 (2021) 440–450
Co_4N nanowire arrays	1.49	44	Angew.Chem. Int. Ed. 2015, 127, 14923 –14927
CoNi-Fe_3N	1.55	34	Small 16(40) (2020) 2003824.
CoN-F	1.506	52.3	Sustainable Energy Fuels, 2021, 5, 3632–3639
CoN-S	1.534	71.2	
CoN-P	1.568	82.1	
Co@Co_3O_4/NC	1.64	54.3	Angew.Chem. Int. Ed. 2016, 55,4087 –4091
CP/CTs/Co-S	1.536	72	ACS Nano 2016, 10, 2342−2348
Co_3O_4/N-graphene	1.54	67	Nature Materials, 10 (2011) 780-786.
CoP/rGO	1.57	66	Chem. Sci., 2016, 7, 1690–1695
N-CG-CoO	1.57	71	Energy Environ. Sci., 7 (2014) 609-616
N/Co-doped PCP//NRGO	1.66	292	Adv. Funct. Mater., 2015, 25, 872-882
Co_xO_y/NC	1.66	-	Angew. Chem. Int. Ed. 2014, 53, 8508 -8512
CoFe/C	1.53	61	Chem. Sci., 2015, 6, 3572-3576
Co_3O_4/BDHC	1.59	47	Adv. Funct. Mater. 2014, 24, 7655-7665
$CoSe_2$-N-Gr	1.55	44	J. Am. Chem. Soc. 2014, 136, 15670-15675
CoNiP/NC	1.46	66	Chin. J. Catal. 39(5) (2018) 982-987.

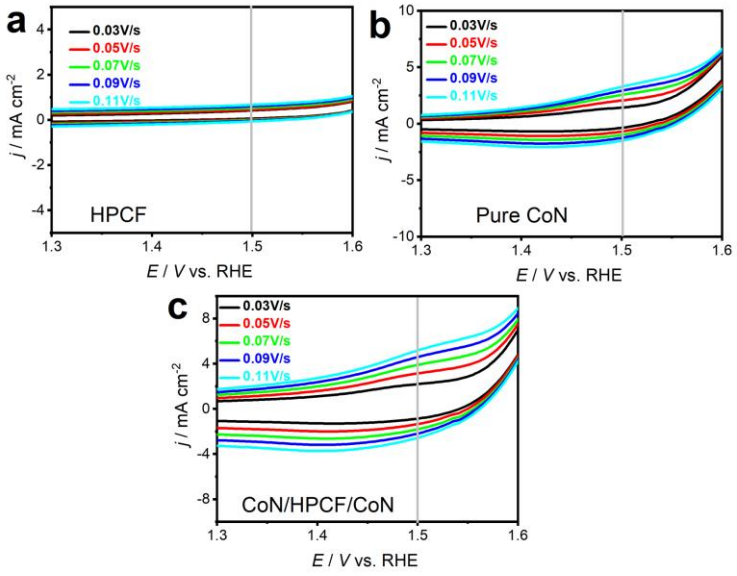

Fig. S11. CV curves recorded at different potential scanning rates from 30 to 110 mV s^{-1} in 1 M KOH solution (between 1.30–1.60 V *vs.* RHE) for the pure HPCF, pure CoN, and CoN/HPCF/CoN hybrid samples.

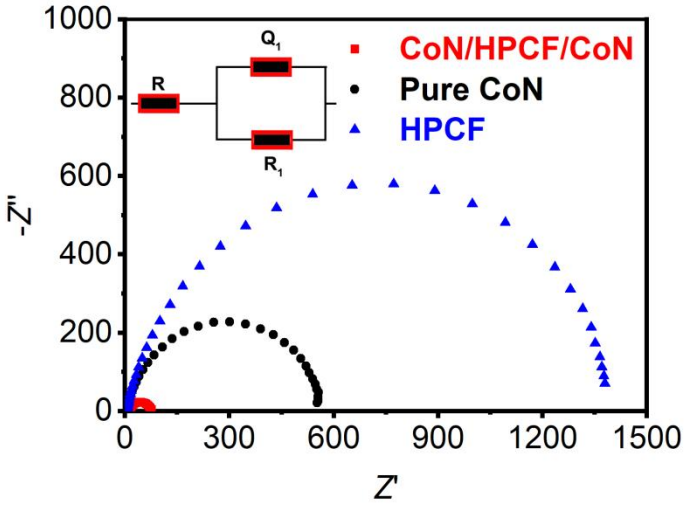

Fig. S12. EIS plots obtained at 1.60 V *vs.* RHE for the HPCF, pure CoN, and CoN/HPCF/CoN samples. The EIS plots were fitted using the electric equivalent circuit (EEC) model showed in inset of Fig. S12**.**

As shown in **Fig. S12**, at 1.60 V *vs.* RHE, the charge transfer resistance (R_{ct}) of HPCF is fairly large (1398 Ω), indicating that the HPCF is poor in active sites. As the OER catalytic activity of CoN, the R_{ct} of pure CoN (537 Ω) is much smaller than HPCF. As the uniformly dispersed active sites of CoN/HPCF/CoN, electron are rapidly formed and transmitted in the OER catalysis, CoN/HPCF/CoN therefore display the smallest R_{ct} of 78 Ω among three control samples, proving the excellent electroconductibility.

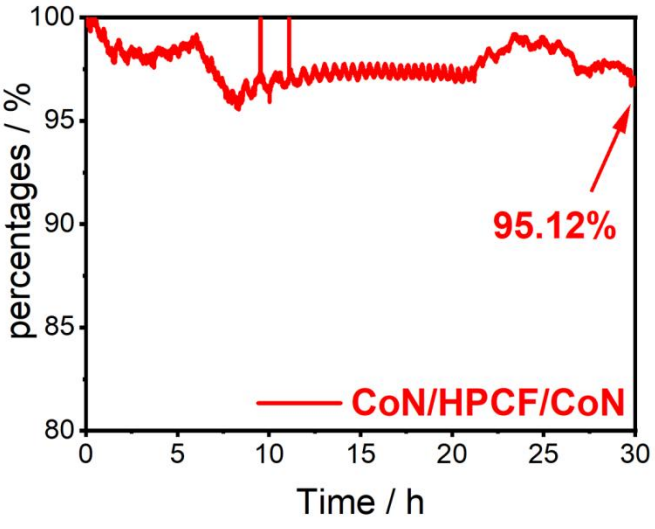

Fig. S13. The chronoamperometry measurement (*I*–*t*) of CoN/HPCF/CoN hybrid sample toward OER carried out at 1.55 V *vs.* RHE for 30 h in 1.0 M KOH .

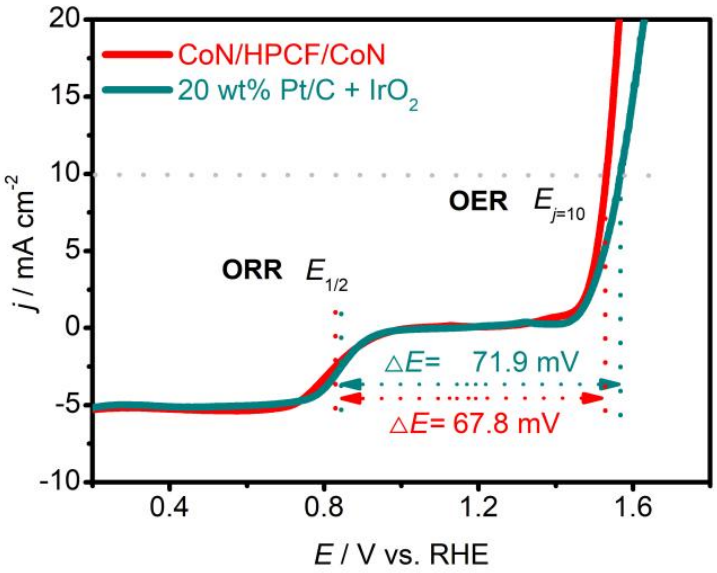

Fig. S14. The oxygen catalytic activities of the CoN/HPCF/CoN hybrid sample and Pt/C-IrO_2 catalysts in 1.0 M KOH with a potential scanning rate of 5 mV s^{-1} at 1600 rpm (from 1.6 to 0.2 V *vs.* RHE).

In order to evaluate and compare the bifunctional electrocatalytic activities CoN/HPCF/CoN hybrid sample and Pt/C-IrO_2 catalysts toward ORR/OER, the overpotential (ΔE) between ORR and OER is the fairly important parameter, which means the loss in efficiency for a cathodic catalyst. In general, the $E_{1/2}$ value is used to quantify ORR activity and the E_{10} value is utilized for measuring the OER activity, thus, $\Delta E = E_{10,\,OER} - E_{1/2,\,ORR}$. In other words, the smaller ΔE value for the same cathode, the better ORR/OER catalyst. As shown in **Fig. S14**, the ΔE value of CoN/HPCF/CoN-CoN/HPCF/CoN is as small as 67.8 mV, which is much smaller than that of Pt/C-IrO_2 catalysts (71.9 mV) and displays the high efficiency of CoN/HPCF/CoN for ORR/OER catalysis.

Table S3 Comparison of the energy density of Zn-air batteries driven by CoN/HPCF/CoN and Pt/C||IrO_2 with recently reported Zn-air batteries.

Catalyst	Peak Power density (mW cm^{-2})	References
CoN/HPCF/CoN	161.6	This Work
Pt/C||IrO_2	140.2	
Co@CoNC-3	122	Chem. Commun., 2018,54, 8190-8193
MnO/Co/PGC	172	Adv. Mater. 2019, 31, 1902339
N-CoS_2 YSSs	81	Adv. Sci. 2020, 7, 2001178
$Co_{1-x}SnO_{3-y}$-$Fe_{0.021}$-A/C	128	Nano Lett., 2023, **23**, 4, 1573–1581
B-$CoSe_2$@CoNi LDH	181.5	Adv. Sci., 2022, 9, 2104522
V-CMO/rGO	145	Adv. Mater. 2023, 35, 2303109
Co@hNCTs-800	149	Nano Energy, 2020, **71**.
Co_3O_4/Co@NCs	123.	Nano Energy, 2020, **77**.

N-CoS_2 YSSs	81	Adv. Sci., 2020, **7**.
ODAC-CoO-30	128.5	Adv. Funct. Mater., 2021, **31**, 2101239.
Fe/Co-N/S-Cs	120.63	Appl. Catal. B-Environ., 2019, **241**, 95-103.
10Co-N@DCNF	184	Angew. Chem. Int. Edit., 2020, **59**, 6122-6127.
CoNi/BCF	155.1	Nano Energy. 2021, **87**.
Co/MnO@N,S-C	120.7	Appl. Catal. B-Environ., 2021, **295**, 120281.
Co/MnO@NC	146	Energy Stor. Mater., 2021, **43**, 42
Co/N@CNTs@ CNMF-800	133	ACS Appl. Mater. & Interfaces, 2020, **12**, 8115.

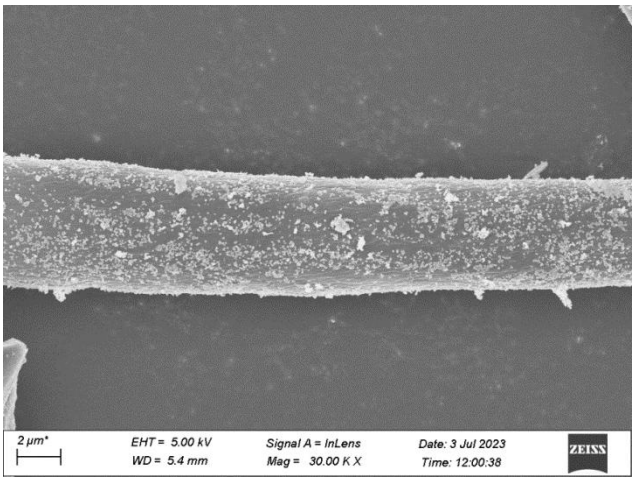

Fig. S15. SEM image of post-cell CoN/HPCF/CoN collected from the air electrode of ZAB after 200 of charge and discharge cycles.

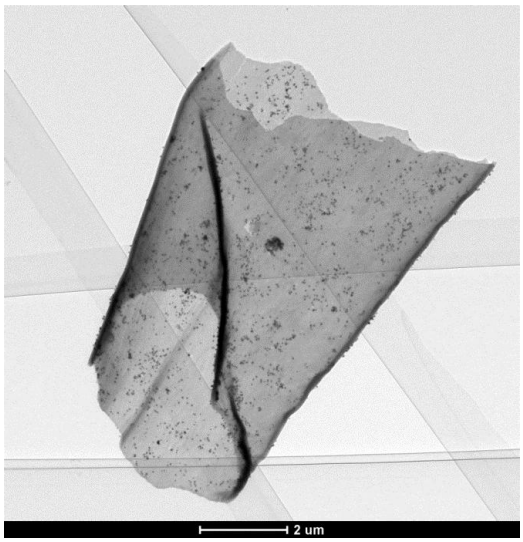

Fig. S16. TEM image of post-cell CoN/HPCF/CoN collected from the air electrode of ZAB after 200 of charge and discharge cycles.

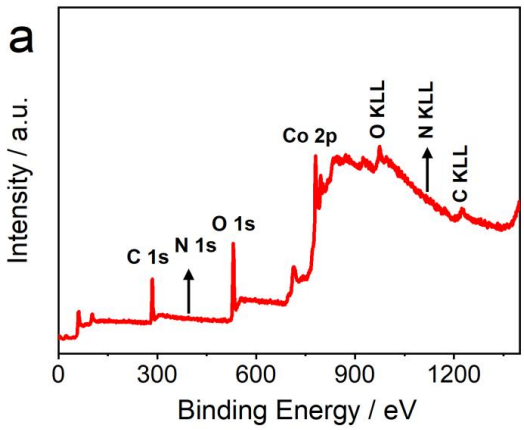

Fig. S17. The XPS survey spectrum of post-cell CoN/HPCF/CoN collected from the air electrode of ZAB after 200 of charge and discharge cycles.

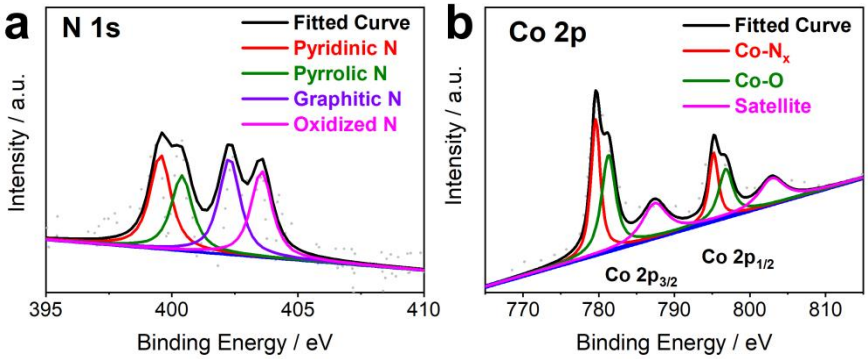

Fig. S18. The high-resolution N 1s **(a)** and Co 2p (**b**) spectra of post-cell CoN/HPCF/CoN collected from the air electrode of ZAB after 200 of charge and discharge cycles.

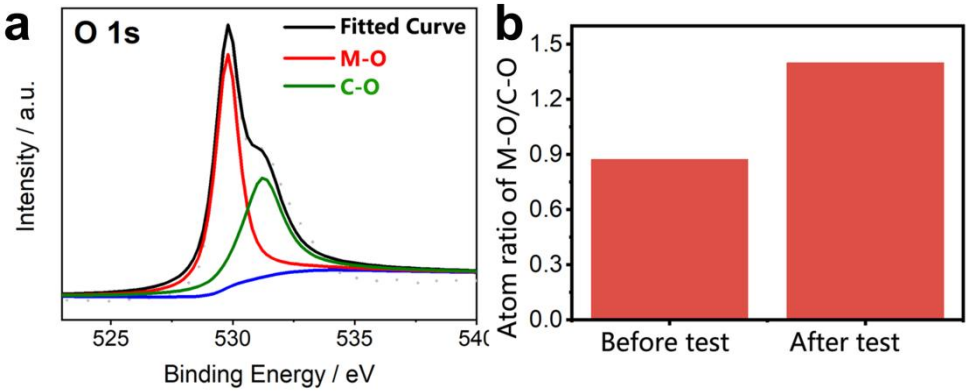

Fig. S19. (a) The high-resolution O 1s of post-cell CoN/HPCF/CoN sample and (**b**) the comparation histogram of atom ratio of M-O/C-O between pristine-CoN/HPCF/CoN catalyst and post-cell CoN/HPCF/CoN collected from the air electrode of ZAB after 200 of charge and discharge cycles.

As shown in **Fig. S19,** after 200 of charge and discharge cycles, more M-O bonds were formed on the surfaces of post-cell CoN/HPCF/CoN in comparation to the pristine-CoN/HPCF/CoN catalyst.

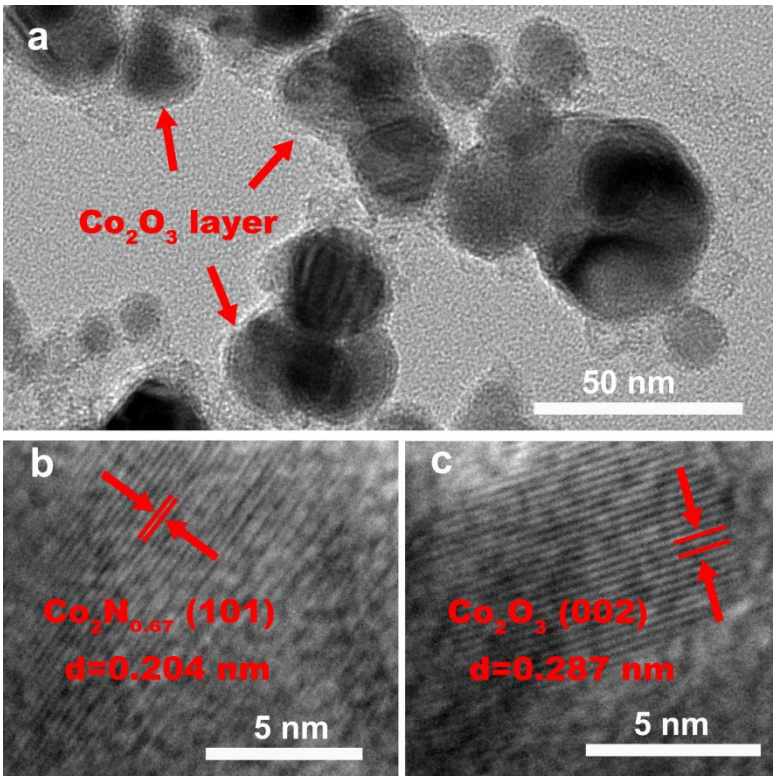

Fig. S20. (a) The HRTEM image various nanoparticles dispersed on post-cell CoN/HPCF/CoN sample. The HRTEM images of inner core (**b**) and outer shell (**c**) of an individual CoN nanoparticle.

As shown in **Fig. S20a**, after 200 of charge and discharge cycles, all CoN nanoparticles were covered by another substance. The HRTEM image of the inner core of an individual nanoparticle reveals a lattice spacing of 0.204 nm (**Fig. S20b**), which is assigned to the (101) facet of $Co_2N_{0.67}$ phase. Nevertheless, the HRTEM image of outer shell of an individual nanoparticle displays a lattice spacing of 0.287 nm (**Fig. S20c**), which is assigned to the (002) facet of Co_2O_3. Combining the high-resolution O 1s spectrum and HRTEM image of post-cell CoN/HPCF/CoN sample, most CoN nanoparticles have turned into the CoN@CoO units after the charge and discharge cycles.

References:

[S1] G. P. Nayaka, K.V. Pai, G. Santhosh, J. Manjanna, J. Environ. Chem. Eng. 4 (2016) 2378–2383.